

Matching the laser generated p bunch into a crossbar- H drift tube linac

A. Almomani, M. Droba, and U. Ratzinger

Institute for Applied Physics, Goethe University Frankfurt, Max-von-Laue straÙe 1, 60438 Frankfurt am Main, Germany

I. Hofmann

GSI / Helmholtz-Institute Jena, PlanckstraÙe 1, 64291, Darmstadt, Germany

(Received 1 December 2010; revised manuscript received 19 December 2011; published 17 May 2012)

Proton bunches with energies up to 30 MeV have been measured at the PHELIX laser. Because of the laser-plasma interactions at a power density of about 4×10^{19} W/cm², a total yield of 1.5×10^{13} protons was produced. For the reference energy of 10 MeV, the yield within ± 0.5 MeV was exceeding 10^{10} protons. The important topic for a further acceleration of the laser generated bunch is the matching into the acceptance of an rf accelerator stage. With respect to the high space charge forces and the transit energy range, only drift tube linacs seem adequate for this purpose. A crossbar H -type (CH) cavity was chosen as the linac structure. Optimum emittance values for the linac injection are compared with the available laser generated beam parameters. Options for beam matching into a CH structure by a pulsed magnetic solenoid and by using the simulation codes LASIN and LORASR are presented.

DOI: [10.1103/PhysRevSTAB.15.051302](https://doi.org/10.1103/PhysRevSTAB.15.051302)

PACS numbers: 29.20.Ej, 52.38.Kd, 41.75.Jv

I. INTRODUCTION

The generation of proton beams from intense laser-plasma interactions with solid targets has been well studied [1–9]. After the implementation of chirped pulse amplification (CPA) [10] technology in modern laser facilities, one can achieve focused intensities approaching 10^{21} W/cm² [11]. Under these conditions, intense protons are accelerated normally from the rear surface of the solid target by quasistatic electric field gradients in the order of TV/m [4–6]. This process of beam formation is called target normal sheath acceleration (TNSA) [3,6]. In contrast to conventional accelerators, the laser generated proton bunch can achieve considerably higher peak currents at beam energies of ten to several tens of MeV [1–9] when compared to state of the art injectors like single ended Van der Graaf accelerators or radio frequency quadrupoles (RFQ's) [12,13]. The important topic for a further acceleration of the laser generated bunch is the matching into the acceptance of an rf accelerator. RFQ's are no more efficient at beam energies around 10 MeV. Because of the available energies drift tube structures are the most adequate choice. There exists long experience at IAP-Frankfurt and at GSI-Darmstadt in the development of highly efficient H -type drift tube accelerators [14]. They seem especially well suited to accept beam bunches like those generated by lasers. A crossbar H -type (CH) structure is suggested because of its high acceleration gradient, β range, mechanical robustness, and high shunt impedance

[14,15] at the relevant injection energies. The motivation for such a combination is to deliver single beam bunches with small emittance values and at an extremely high particle number per bunch.

Laser-proton acceleration offers unique features like very high acceleration gradients of the order TV/m, extremely small longitudinal and transverse emittances due to short time pulses (ps range), and small source spots (few tens of μ m) as well as a high yield of particles (10^{12} – 10^{13} protons per shot) [2,3,7,8]. The results from laser experiments, like those performed in 2008 with the petawatt high energy laser for heavy ion experiments (PHELIX) at GSI [7–9,16] and from simulations performed by the WARP code [17], show that there are some restrictions with respect to a postacceleration of the generated bunches. In these experiments, a laser beam of about 700 fs duration was focused by a copper parabola mirror on a beam spot of about $170 \mu\text{m}^2$ (FWHM) which results in a power density of about 4.5×10^{19} W/cm² [9]. For the reference energy of 10 MeV, the yield within ± 0.5 MeV was exceeding 10^{10} protons (Fig. 1) [16]. To

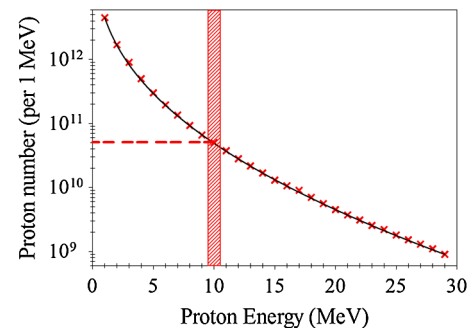


FIG. 1. Dependence of differential particle yield on energy for PHELIX experiment [16].

Published by the American Physical Society under the terms of the [Creative Commons Attribution 3.0 License](https://creativecommons.org/licenses/by/3.0/). Further distribution of this work must maintain attribution to the author(s) and the published article's title, journal citation, and DOI.

compare this number with the conventional currents, the sum current of these bunches might add up to 500 mA beam current if every bucket would be filled with that proton number at 325 MHz. Proton spectra are characterized by a large divergence (23° half angle for energies around 10 MeV). This divergence was found to decrease with increasing energy down to 8° half angle for 29 MeV [8,16].

In order to catch the protons around 10 MeV, a pulsed solenoid could be used as the first focusing element with high pulsed field strengths (see next sections). The particle simulations of the generated proton pulse through the matching section were done by a new 3D code—LASIN (laser injection). This code, which was developed at IAP-Frankfurt, is used for multiparticle tracking through the solenoid magnetic field including fringing fields. For beam simulations along the CH-accelerating structure the LORASR code was used [18,19].

II. LASIN CODE

The LASIN code is developed for multispecies (electrons, protons, and ions) beam tracking through a solenoidal magnetic field with high space charge forces and at rapidly varying geometric bunch dimensions (from $10\ \mu\text{m}$ –5 cm transversely along a longitudinal drift of about 50 cm). The magnetic field is calculated by the Biot-Savart solver using a numerical integration scheme from a given distribution of current elements, including conductors and particle contributions. At every exact particle position at a given time step, B field is calculated accordingly.

In case of space charge forces, the charge density is integrated on a cylindrical mesh from a particle distribution by particle in cell techniques [20]. Afterwards, the Poisson equation is solved numerically by the iteration method BICGSTAB (biconjugate gradient method stabilized) [21] on the mesh resulting in the potential distribution. For the tracking algorithm the electric field is interpolated at the particle position.

A symplectic middle step scheme [22] in Cartesian coordinates is used to follow the particle motion in given fields.

The code is implemented at the Frankfurt Center for Scientific Computing CSC cluster by fully exploiting the parallel processing capabilities. Typically, 50 processors and up to 10^7 macroparticles are used in proton tracking simulations from the target (TNSA) to the CH-accelerating structure. For optimization purposes and memory requirement reduction the sparse format of stored vectors and matrices is used.

III. PULSED MAGNETIC SOLENOID

A. Magnetic solenoid simulations

Beam dynamics simulations through the pulsed magnetic solenoid for a proton bunch with energies $10\ \text{MeV} \pm \Delta E$ are described in the following.

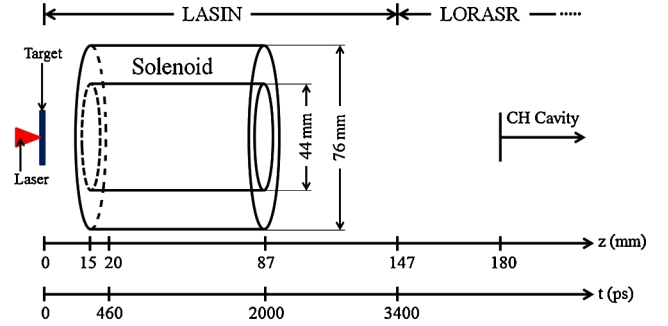


FIG. 2. Schematic view of the laser target, the focusing solenoid, and the drift to the rf linac. The longitudinal axis is marked in mm and in ps time of flight for a 10 MeV on axis proton. Additionally, the range of LASIN and LORASR code based simulations are indicated.

The well-known 4D Kapchinski-Vladimirski distribution was generated as a very first particle distribution for the simulations. The main goal was a check of chromatic and geometric effects taking into account higher order aberrations [8,23]. To simulate the solenoidal magnetic field, 33 circular windings with an inner diameter of 44 mm, an outer diameter of 76 mm, and a total length of 72 mm were defined (Fig. 2). The distance between target and geometric coil entrance was set to 15 mm and corresponds to the performed experiments.

The 10 MeV p bunch in this lens layout needs a magnetic field level of about 18 T in order to focus directly into a CH drift tube linac (DTL) at a distance of about 210 mm from the target. The solenoidal field extension along z is shown in Fig. 3. The cyan lines represent the geometrical size of the solenoid while the brown line represents the source position. The magnetic field in the target area is about 6 T (Fig. 3, left), which means that the protons (and the comoving electrons) are produced in a relatively high magnetic field. That means the hard edge solenoid approximation is insufficient for our study and the effect of fringing fields must be taken into account as was done in LASIN.

B. Chromatic and geometric aberrations

In order to estimate the chromatic and geometric effects for the pulsed magnetic solenoid, the beam dynamics simulations were performed for a beam with variable input divergence ($\alpha: \pm 45\ \text{mrad}, \pm 90\ \text{mrad}$ and $\pm 180\ \text{mrad}$) and with different momentum spreads up to $\pm 10\%$, at negligible space charge forces.

The particle tracking (without space charge) immediately behind the target is performed in the time domain with time steps of 10^{-11} s typically. This corresponds to steps in space of about $440\ \mu\text{m}$ along the drift axis.

The chromatic emittance for a given solenoid and spot radius obeys the scaling

$$\varepsilon_c \propto \alpha^2 \Delta p / p, \quad (1)$$

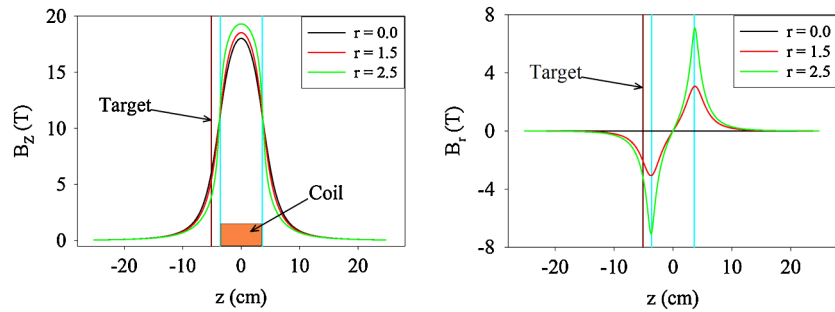


FIG. 3. Longitudinal (left) and transverse (right) components of the solenoidal field along the axis for different radii in cm; the geometric length of the solenoid (cyan lines) as well as the target position (brown line) are marked.

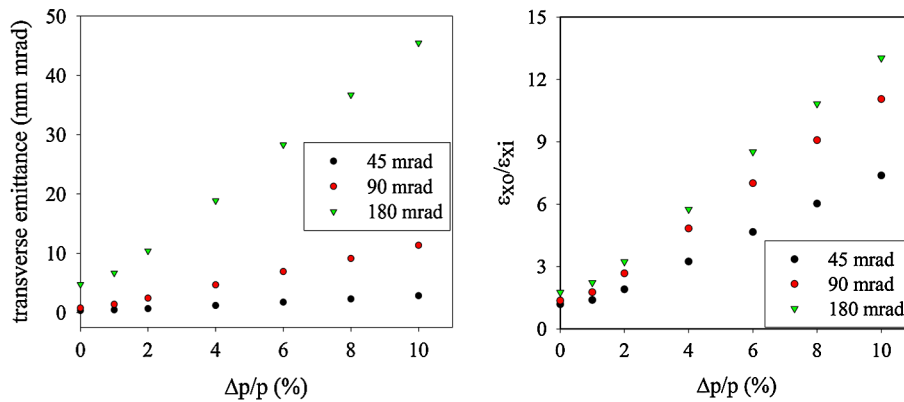


FIG. 4. Output rms emittance in x - x' versus $\Delta p/p$ (left); output to input rms-emittance ratio in x - x' plane versus $\Delta p/p$ (right) at different opening angles, 210 mm behind of the target.

where α is the opening angle and $\Delta p/p$ is the momentum spread [8,24]. ε_c dominates the usually smaller input emittance and becomes the effective emittance (see Figs. 4 and 5). The magnetic field level 210 mm behind the target is below 1% of the maximum field. The resulting emittance at that position depends on the initial beam divergence as well as on the momentum spread. The influence of both effects at that position can be seen by Fig. 4, where three cases for the beam divergence are plotted.

The predicted linear behavior is confirmed between 1% and 10% momentum spread (Fig. 4, left). The relative emittance growth factors resulting from geometric and chromatic aberrations are shown in Fig. 4 (right).

LASIN includes nonparaxial effects, which leads to the s-shaped distortion of the output distribution even for monoenergetic beams (Fig. 5, left). The effect is quite pronounced at beam divergence as large as ± 180 mrad, which results in a filling of 45% of the solenoid aperture.

The chromatic effect of the solenoid is shown by Fig. 5 (right), resulting in a bow tie like emittance shape.

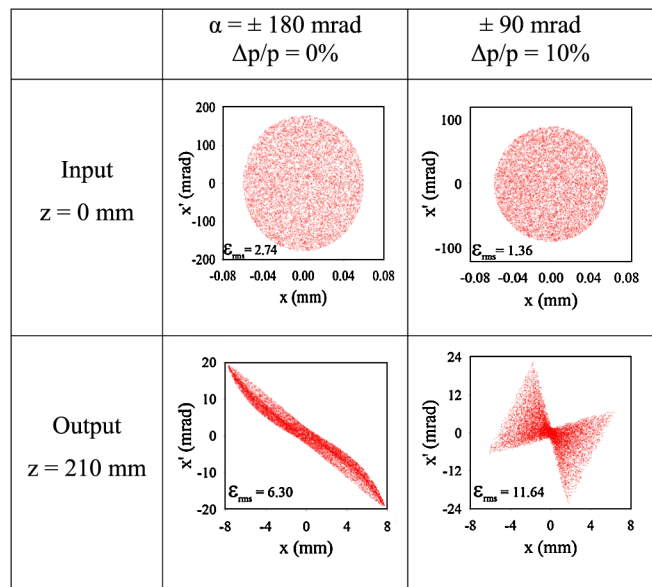


FIG. 5. Input and output distributions in x - x' for a monoenergetic beam with a divergence of ± 180 mrad (left), and for a beam with $\Delta p/p = \pm 10\%$ at ± 90 mrad (right).

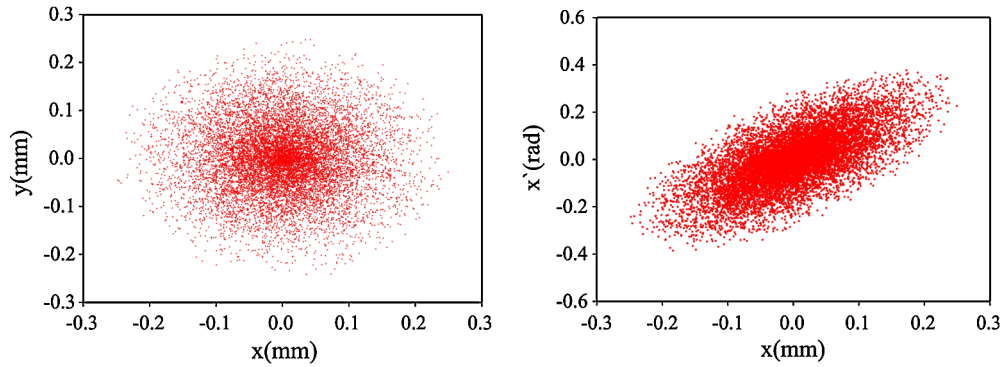


FIG. 6. The xy (left) and xx' (right) projections of the 10 ± 0.5 MeV fraction of a simulated proton pulse after 10 ps; $\varepsilon_{rms} = 6.56$ mm mrad.

C. Space charge effect

The proton bunches are expected to be space charge neutralized to a high degree behind the target foil. Besides the mesh resolution close to the target, details of the initial proton and electron distributions in phase space have to be chosen properly. Especially, the huge electric fields caused by charge separation in the presence of the solenoidal field result in mesh parameter conditions: Courant stability criteria for numerical explicit schemes require that $v \times \Delta t_{\text{mesh}} < \Delta z_{\text{mesh}}$, resulting in a small time step. Because of the fact that the maximum occurring electric field is a dynamical variable, several preliminary test simulations were needed to find an optimum mesh setting. The total internal energy (potential plus kinetic energy of all particles) was calculated as a control parameter to check conservation properties and to distinguish between numerical and physical effects.

These preliminary simulation checks and optimum use of the available cluster capabilities resulted in the following strategy, which divides the transport line into 4 sections III C 1–III C 4, simulated by LASIN.

1. *Input distribution and transport 0–10 ps.*—In the following, an isothermal expansion model during the first 10 ps with starting from a Gaussian 2σ density distribution was assumed. The parameter “initial source radius” was varied from $280 \mu\text{m}$ at 5 MeV to $70 \mu\text{m}$ at 15 MeV continuously, and the angular divergence was varied from 400 to 140 mrad accordingly. The dependence of initial parameters on energy is fitted to the measured data from the PHELIX laser experiments [25]. An initial energy spectrum as large as 10 ± 5 MeV was assumed in the simulations. It should be mentioned that this energy range is 10 times larger than the energy band of 10 ± 0.5 MeV, which was chosen for rf postacceleration (see Sec. V). This concept should result in an acceptable accuracy of the simulation results for the output energy range of interest. The maximum macroparticle number used in these simulations was limited to 10^7 . Electrons were chosen to be comoving with the protons and with a density resulting in 100% space charge compensation at the starting position.

The resultant proton and electron distribution after 10 ps drift time was used as input distribution into the following section.

2. *Transport 10–40 ps.*—The starting distribution of the interesting energy range $10 \text{ MeV} \pm 0.5 \text{ MeV}$ for rf post-acceleration is shown in Fig. 6. The longitudinal starting position of the pulse center at $t = 10$ ps is about $400 \mu\text{m}$ from the target surface.

The initial density profile of the protons in the transverse planes is Gaussian (see Fig. 7).

The cylindrical mesh dimensions $\Delta r = 4 \mu\text{m}$, $\Delta z = 2 \mu\text{m}$, $\Delta\phi = 0.21$ rad, and the time step

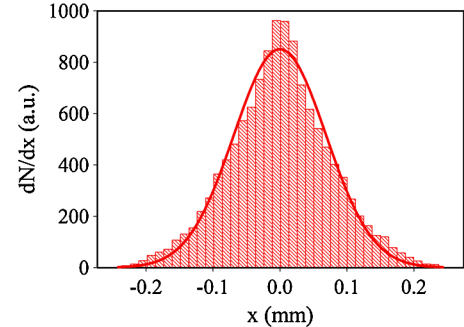


FIG. 7. Transversal density profile of the particle pulse.

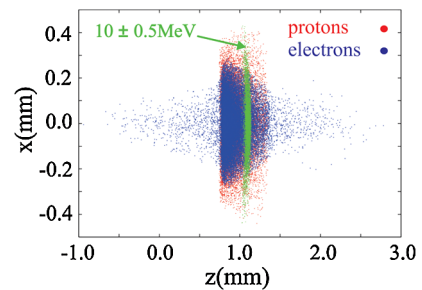


FIG. 8. z - x projection of the particle distributions after 25 ps. The action of the magnetic solenoid fringing field is seen already. Particle energies of interest for acceleration are marked in green.

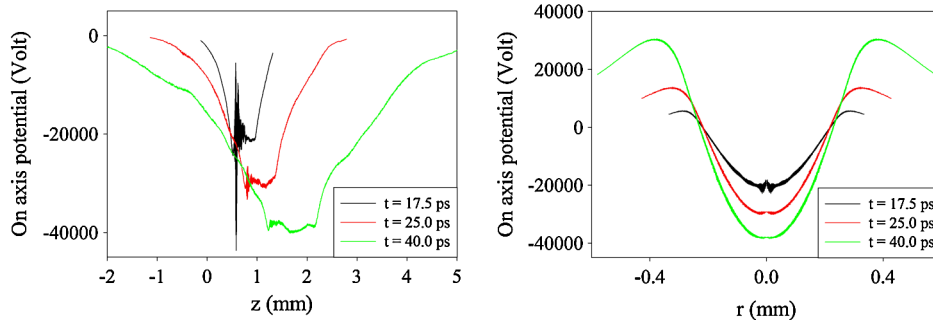


FIG. 9. Potential curves in longitudinal (left) and transversal (right) directions at three different positions along z . At $t = 40$ ps, the space charge potential is reaching a maximum.

$\Delta t = 2.5 \times 10^{-14}$ s were chosen. Because of the fringing field of the focusing solenoid in the target region, electrons are transversally captured. On the contrary, the protons with their large transversal momentum can expand radially (see Fig. 8).

Because of the charge separation caused by solenoid fringing fields, the on axis electron density leads to a negative on axis potential reaching about -40 kV after 40 ps (see Fig. 9).

As a consequence, the electrons can escape and are accelerated longitudinally. Subsequently, the potential drops down and electrostatic energy is converted to the kinetic energy of the particles. The rapid thermalization

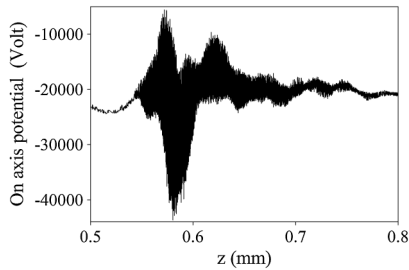


FIG. 10. Detail of the potential curve (from Fig. 9) after 17.5 ps in the longitudinal direction. The plasma oscillation has a higher potential fluctuation at lower z positions, where the simulated particle density is higher.

process of the longitudinal electron distribution along the magnetic field was observed. Generally, this fact is demonstrated by the potential behavior as shown in Fig. 9. An occurring plasma oscillation at $t = 17.5$ ps (Figs. 9 and 10) is almost damped at $t = 40$ ps. For comparison, at a typical electron density of 10^{21} m^{-3} , the plasma frequency has an oscillation period of 2 ps. The potential at $t = 40$ ps is reaching almost constant values along the z axis within the propagating proton bunch: The electron kinetic energy distribution (Fig. 11, left) is changed to the Maxwellian form.

After 25 ps some of electrons start to escape from the proton bunch and are accelerated to high energies in $+z$ and $-z$ directions. Two peaks are now evident in the distribution function (Fig. 11, right).

The proton kinetic energy distribution stays unchanged within the first 40 ps (Fig. 16). The growing pronounced charge separation is stimulated by the big initial beam divergence.

The overall energy conservation was monitored and was proven down to the 10^{-4} level.

3. *Transport 40–460 ps.*—Because of the relaxing space charge forces, the cylindrical mesh could be adapted to $\Delta r = 45 \mu\text{m}$, $\Delta z = 45 \mu\text{m}$, $\Delta \phi = 0.21$ rad with the time step $\Delta t = 3.5 \times 10^{-13}$ s. The small time step is due to the electron gyration in the magnetic field. The transverse proton expansion after propagating 2 cm along the beam

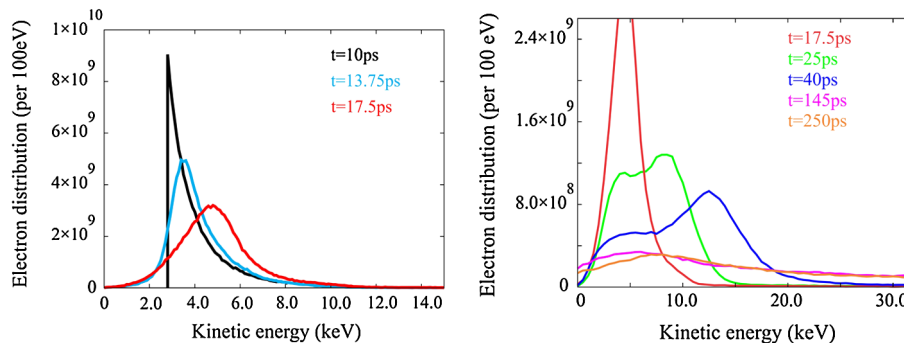


FIG. 11. Time evolution of the electron energy distribution. The right picture for $t \geq 17.5$ ps has different scales.

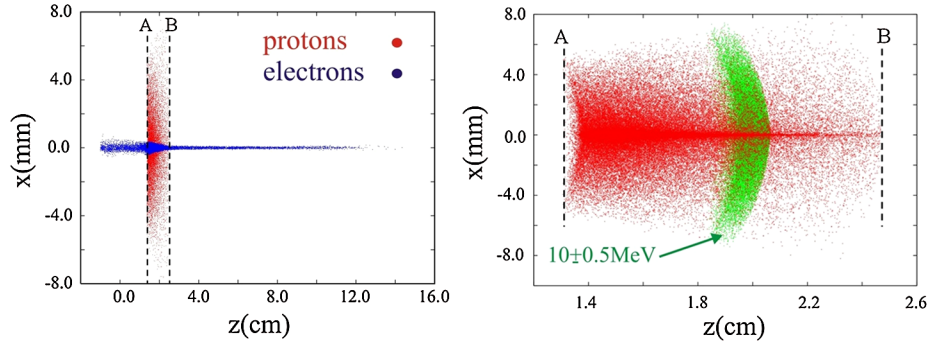


FIG. 12. Proton (red) and electron (blue) distribution in the z - x plane after 460 ps. Electrons are accelerated axially by their own potential. The detail AB containing the whole proton distribution is shown on the right. The green marked area corresponds to the protons with $10 \text{ MeV} \pm 0.5 \text{ MeV}$.

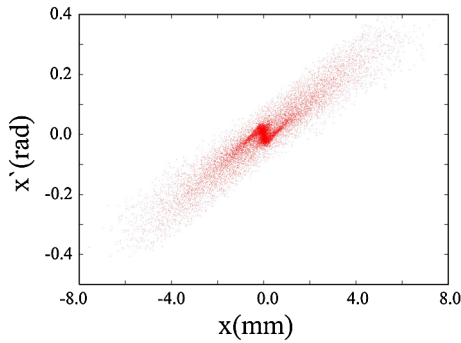


FIG. 13. The x - x' phase space projection of the whole transported proton spectrum with $10 \text{ MeV} \pm 5 \text{ MeV}$ at 460 ps. The pronounced core structure is dominated by the lower energy protons (compare with Figs. 12 and 15).

axis is shown by Fig. 12. The electric potential is relaxing to the -5 kV level.

An electron influence on the proton distribution is clearly demonstrated in the x - x' phase space projection for the whole energy spectrum $10 \text{ MeV} \pm 5 \text{ MeV}$ (Fig. 13). The central part of the proton distribution ($r < 500 \mu\text{m}$) is strongly focused due to the pronounced electron radial focusing force close to the axis. Consequently, the slope of the core distribution in the

phase space projection differs strongly from the proton distribution at larger radii.

The peaked transversal proton distribution containing about 30% of all macroparticles within a radius of $500 \mu\text{m}$ contains the whole energy spectrum.

The transverse distribution of the $10 \text{ MeV} \pm 0.5 \text{ MeV}$ proton fraction is shown in Figs. 14 and 15.

The phase space distributions in x - y and x - x' show again a focused central core.

The proton kinetic energy spectrum after 460 ps is only slightly changed, mainly within the lower energy side (Fig. 16). The longitudinal proton bunch position after 460 ps is just at the entrance of the solenoid.

4. *Transport 460 ps–3.4 ns.*—In the following simulation the influence of comoving electrons was neglected because the electron and proton phase spaces are well separated now (see Fig. 12): The maximum radial electric field at $t = 460 \text{ ps}$ reached the 10^7 V/m level at $500 \mu\text{m}$ radius. This corresponds to the rigid rotor equilibrium between magnetic and electric focusing forces in case of the proton distribution. This fact could be expressed by

$$\omega_c = \frac{e \cdot B_z}{m_p} = \frac{E_r}{B_z \cdot r} = \omega_E, \quad (2)$$

where the cyclotron frequency on the left is equal to the $\vec{E} \times \vec{B}$ drift frequency on the right.

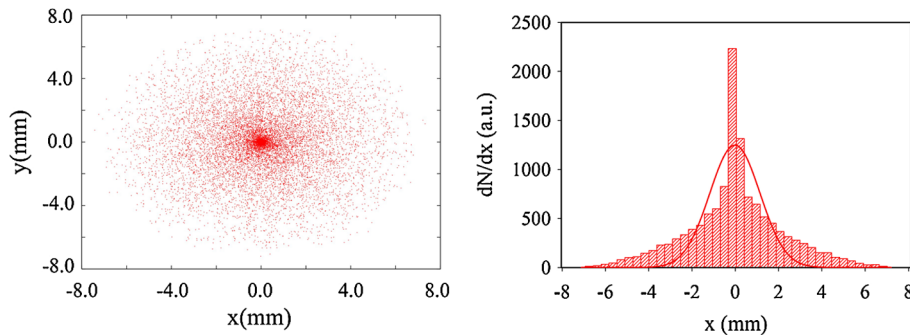


FIG. 14. Transversal proton distribution for the energy band $10 \text{ MeV} \pm 0.5 \text{ MeV}$ after 460 ps.

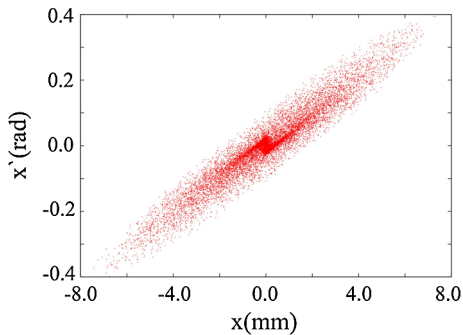


FIG. 15. Proton distribution $x-x'$ for the energy band $10 \text{ MeV} \pm 0.5 \text{ MeV}$ after 460 ps. The local influence of electrons coming on the axis is seen at $|x| < 0.5 \text{ mm}$.

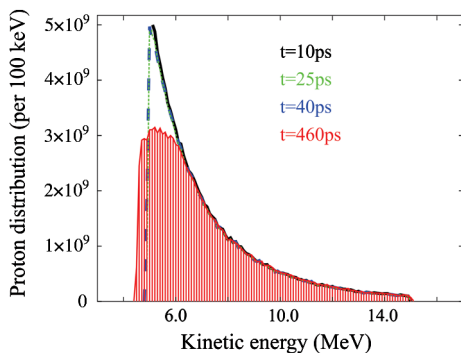


FIG. 16. Proton spectral distribution development within the first 460 ps. The shape is changing mainly at the low energy end.

After 460 ps, the focusing electric forces due to the electron distribution will be vanishing and the magnetic force becomes dominant. No more additional proton accumulation on axis is possible and the proton distribution will only rotate near the axis.

The radial electric force due to the electron column reached the 10^6 V/m level in the outer part ($r > 1 \text{ mm}$) of the proton distribution, and its contribution is then decreasing proportional to $1/r$ outside. Estimating the momentum transfer to the proton distribution after 460 ps

down along the whole solenoid results in angular corrections below the 1% level.

The time step was set to $\Delta t = 2.5 \times 10^{-11} \text{ s}$ and mesh cells to $\Delta z = 1 \text{ mm}$, $\Delta r = 88 \mu\text{m}$ dimensions.

The resulting proton distribution as described in Sec. III C 3 is now transported along the remaining length of the solenoid and up to $t = 3.4 \text{ ns}$. This corresponds to a drift of 60 mm behind the solenoid for the 10 MeV protons (Fig. 17). The low energy proton fraction is concentrated on the left, approaching a waist, while the high energy protons on the right show a central, focused core caused by the electrons in the early stage of beam motion. The distribution of the particles with $10 \text{ MeV} \pm 0.5 \text{ MeV}$ clearly shows the dominance of the chromatic aberration as discussed in Sec. III B and displayed in Fig. 5.

A maximum potential of +14 kV after the propagation time of 3.4 ns was reached on axis at position $z = 11 \text{ cm}$. A potential level of about 4 kV was detected for the energy of interest at 10 MeV, $z = 15 \text{ cm}$. It has to be noted that this potential is now acting on protons only. The simulation with LASIN ends at this point and the fractional distribution (green marked area, Fig. 21) was adapted as input distribution for the following linac simulation. The relative transverse and longitudinal rms-emittance growth could be calculated as the ratio between the output to the input rms values and it was about 10 at the end of the solenoid transport ($\epsilon_{\text{rms,out}}/\epsilon_{\text{rms,in}} \approx 10$).

IV. HIGH CURRENT PROTON BEAM ACCELERATION BY CH-TYPE CAVITIES

In this section, the crossbar H -mode DTL (CH-DTL) will be discussed briefly. For the continuation of matching and acceleration studies see Sec. V.

The CH-DTL structure is a multicell drift tube cavity (Fig. 18) developed at IAP-Frankfurt [14,26,27], operating in the TE_{210} mode (H_{210}). The structure has features like high shunt impedance, high acceleration gradients, and robustness in design. Because of that, it is well suited for pulsed high intensity proton acceleration with β ranging from 0.1 to 0.5 [27]. The FAIR proton linac will use the CH-type structure [28–30].

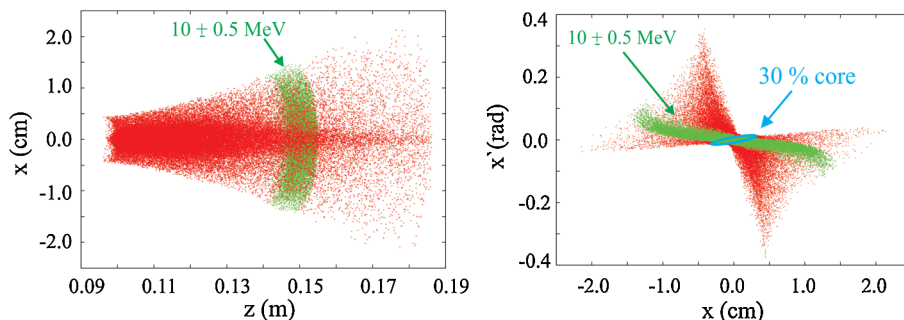


FIG. 17. (Left) $z-x$ proton distribution after the solenoid. The longitudinal position is correlated to the individual proton energies. (Right) $x-x'$ distribution for the same propagation time $t = 3.4 \text{ ns}$. The green marked area corresponds to the energy of interest (see also Fig. 25 for a more detailed view).

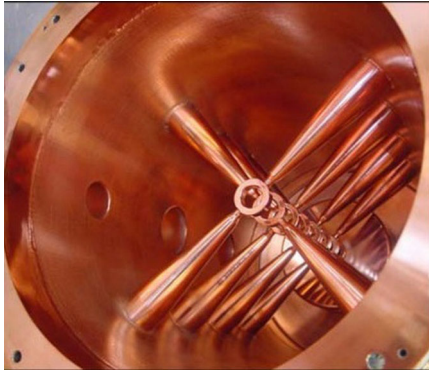


FIG. 18. A copper plated CH-DTL structure.

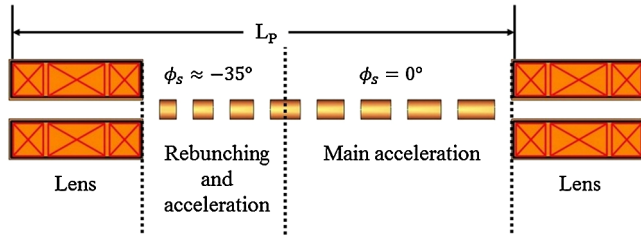


FIG. 19. A schematic view of the CH-DTL, showing the separated function concept of the KONUS-beam dynamics.

The CH-DTL is characterized by slim drift tubes without internal focusing elements which allow the construction of quite compact cavities, having higher shunt impedance when compared to the conventional rf structures like an Alvarez-type DTL based on FODO lattices. A schematic of the CH-DTL applying the KONUS-beam dynamics [14,31] is shown in Fig. 19: One KONUS period

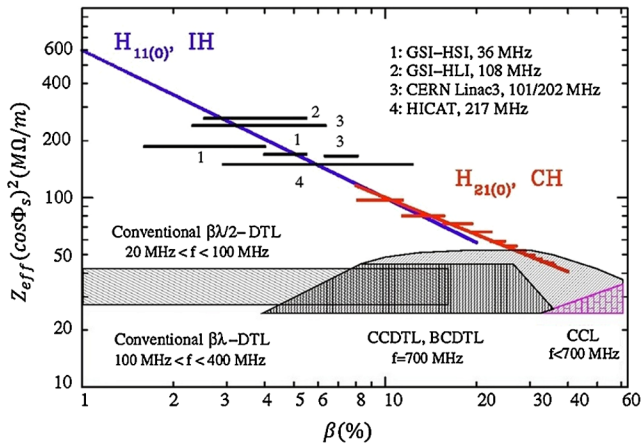


FIG. 20. Effective shunt impedance for different rf structures including the transit time factor T and the synchronous phase φ_s as a function of the particle velocity $\beta = v/c$. The black horizontal bars represent some realized interdigital H -mode (IH)-DTL's while the blue line represents the expected shunt impedance from IH cavities. The red line represents the expected shunt impedance of the room temperature CH cavities for the GSI-FAIR 70 MeV, 70 mA proton linac [26].

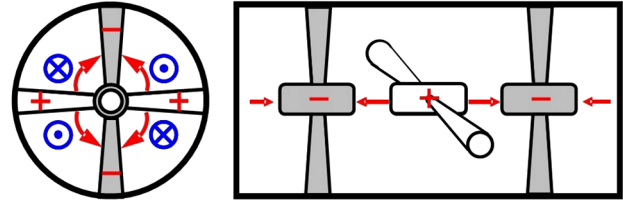


FIG. 21. Schematic diagram of a crossbar H -mode structure (CH) showing the electric fields in red and the magnetic fields in blue (courtesy of Rudolf Tiede).

L_p consists of a transversally focusing lens, a longitudinally focusing rebunching section with a negative synchronous rf phase, and a main acceleration section defined by a $\varphi_s = 0^\circ$ synchronous particle. The bunch is injected into the latter section with a surplus in energy against the synchronous particle for longitudinal stability reasons.

Figure 20 shows the effective shunt impedance $Z_{eff} = Z_0 T^2 \cos^2 \varphi_s$ as a function of the particle velocity $\beta = v/c$, where T is the transit time factor and φ_s is the synchronous phase.

Because of the lack of internal focusing elements in the rf cavity, the adaption of slim drift tubes for the H -type DTL is possible. This allows reaching very high effective field gradients up to 10 MV/m [32] at high robustness against multipacting and sparking.

It should be noted that the orientation of each neighboring stem under 90° not only produces the axial electric fields in the CH cavity (Fig. 21), but also results in mechanically robust cavity geometry.

With respect to laser accelerated beams, the capability of the CH cavity for high current beams has been investigated. Beam bunch simulations have demonstrated that a current up to 500 mA can be accelerated successfully and loss free along the cavity. This corresponds to 10^{10} protons per bunch as offered by the laser source (see Fig. 1). A detailed description of the beam matching and acceleration by a dedicated CH linac is given in Sec. V.

V. RF POSTACCELERATION OF THE LASER GENERATED PROTON PULSE BY A 40 MEV CH LINAC

A high intensity laser generated proton bunch might be injected into a linac at energies of ten to several tens of MeV for further acceleration. The laser generated proton bunch has small emittance values initially when compared to conventional accelerators, at an extremely high proton number per bunch. To compare the beam dynamics in each bunch with conventional bunch trains, we compare the beam current resulting from a cw linac operation with all rf buckets filled with the same particle number. The resulting equivalent beam current to be used for beam dynamics calculation is then

$$I_b = N_b \cdot f \cdot e. \quad (3)$$

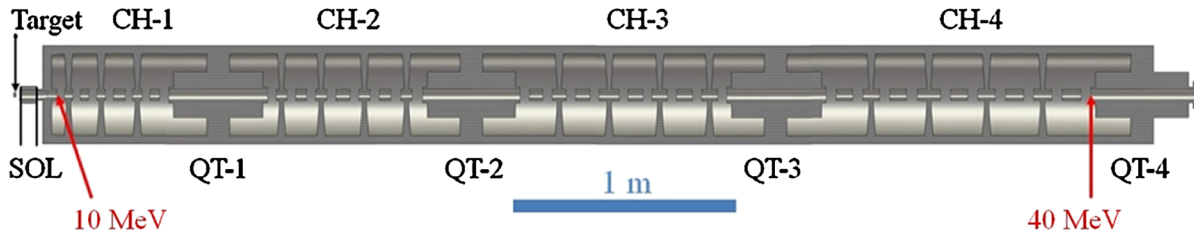


FIG. 22. 3D view on the proposed CH-DTL consisting of four rf cavities separated by triplet quadrupoles. In front of the first cavity, the pulsed solenoid is located and the distance between the end edge of the solenoid and the center of the first gap is 103 mm.

For example, at $N_p = 10^{10}$, $f = 325$ MHz the average current $I_b = 0.52$ A. This may be compared to 100 mA beam current which is state of the art in conventional injector techniques.

Reference [33] is an early publication about the rf acceleration topic: A 7 MeV laser generated proton pulse is matched by 1.8 m long matching section with five quadrupoles to a 6 m long 7 MV Alvarez-type DTL.

In the present work, the capabilities of a CH linac for the acceleration of laser generated proton pulses are investigated.

A. Dedicated CH-linac design for the laser accelerated protons

The layout of the CH-DTL was performed in two main steps. At first, a 500 mA equivalent beam current design was developed. In a second step, the linac layout as presented below was finally defined by optimizing the beam transport for the laser generated pulse. Indeed, the initial beam emittance values of the laser accelerated protons are much smaller than the values for conventional linacs, but as a consequence the space charge effects become much bigger (Sec. III C 2). It is shown in the following that the beam

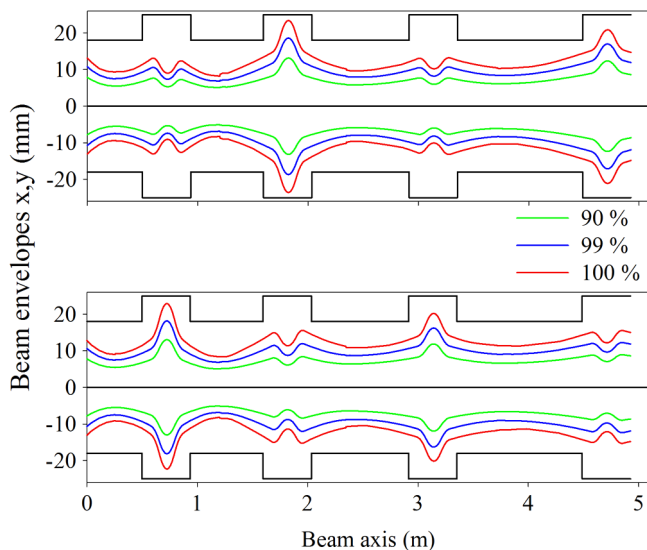


FIG. 23. Transverse 90%, 99%, and 100% envelopes at 500 mA beam current. Black lines indicate the aperture.

emittance of the laser accelerated bunch in front of the linac was even too big for full transmission. The 500 mA CH-DTL design was performed at IAP-Frankfurt and is shown in Fig. 22. The bunch transport along the matching section was simulated using the LASIN code (see Sec. II). The continuation of beam dynamics studies for the longitudinal and transverse planes along the DTL were performed by the LORASR code.

This design consists of four CH-type cavities with gap numbers varying from 7 to 10 gaps and operating at 325 MHz, to accelerate up to 10^{10} protons per bunch from 10.05 to 40.03 MeV. The total length is 5.10 m and the average accelerating gradient per cavity varies from 7.00 to 12.61 MV/m. In order to get a robust longitudinal bunch focusing, high gap voltages of typically 1 MV are applied. The calculated effective voltage distribution along the CH structure is roughly uniform within each section and varies from 0.92 to 1.08 MV per gap.

Because of the fact that the transverse focusing period is much longer than in a conventional FODO structure, and in order to reduce beam losses, the length of the first cavity was limited to 7 gaps only.

Two injected beam distributions were analyzed for this design: The matched case which is a numerically generated waterbag distribution with rms-emittance values close to the linac acceptance (compare aperture filling in Fig. 23), and the laser accelerated case with a proton distribution as simulated in Sec. III C.

1. Matched beam case

The matched beam parameters at 500 mA are summarized in Table I, where the input values are given 40 mm in front of the first gap center (compare to $z = 147$ mm in Fig. 2). The particles were accelerated to the exit without any losses.

TABLE I. Normalized rms-emittance values for the input and output distribution with 500 mA beam current.

Emittance	Input	Output
Transverse/mm mrad	x : 3.85 y : 3.85	4.08 4.06
Longitudinal/keV ns	5.37	6.68

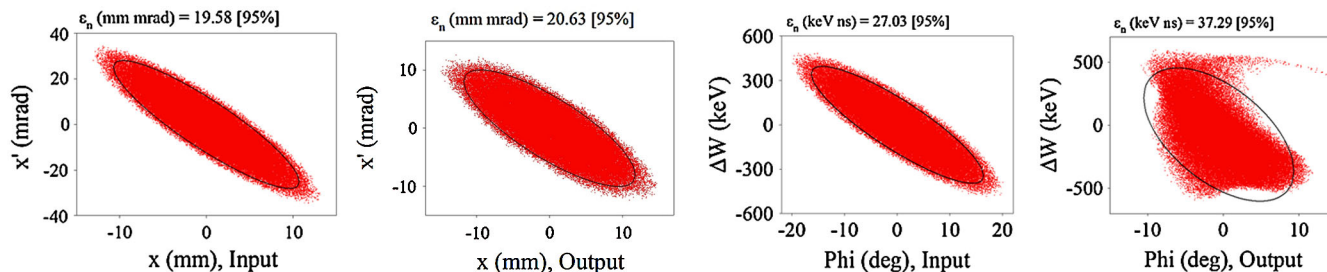


FIG. 24. Transverse (left) and longitudinal (right) particle distribution at entrance and exit of the CH-DTL section at 500 mA equivalent beam current. The input and output energies of the CH-DTL were 10 and 40 MeV, respectively. Normalized emittance values are relevant for the plotted 95% ellipses.

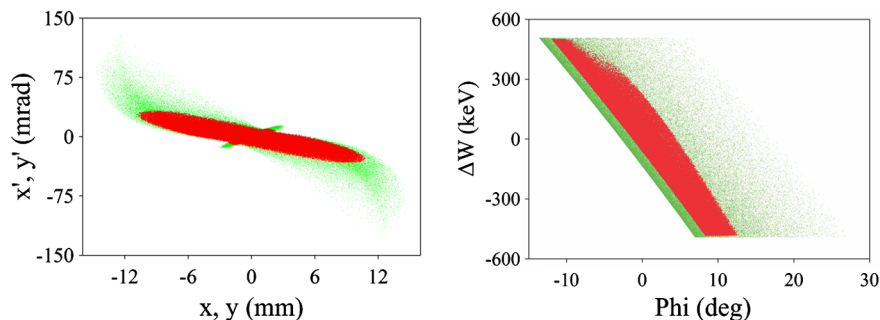


FIG. 25. Laser generated particle distribution in transversal (left) and longitudinal (right) planes at the DTL entrance within an energy range $10 \text{ MeV} \pm 0.5 \text{ MeV}$ in green (identical with the green distribution of Fig. 17, right). The red 72% subset falls within the transverse CH-DTL acceptance area and is used for DTL beam dynamics simulations.

The rms-emittance growth rates along the linac are less than 25% in the longitudinal plane and less than 6% in the transverse planes.

The transverse 90%, 99%, and 100% beam envelopes at 500 mA equivalent beam current can be seen in Fig. 23. The magnetic field gradients of the quadrupoles are ranging up to 50.5 T/m at quadrupole aperture radii of 25 mm. The particle distributions at entrance and exit in transverse and longitudinal planes are shown in Fig. 24 for 10^6 macroparticles.

These simulations demonstrate the capability of the CH structure to accelerate high current beams.

2. Laser accelerated beam case

The laser generated proton bunch was simulated by LASIN along the pulsed magnetic solenoid (Sec. III C) and down to a position 40 mm in front of the first DTL gap. After that, the particle distribution is reduced to the energy window $10 \text{ MeV} \pm 0.5 \text{ MeV}$ corresponding to the longitudinal DTL acceptance. 6×10^9 protons are contained in this bunch, corresponding to a linac current of 300 mA, and plotted green in Fig. 25. The red particles fall into the simulated transverse DTL acceptance as derived from the matched beam case above. In consequence, only 72% of all particles within $10 \pm 0.5 \text{ MeV}$ are accepted by

the DTL. The other particles are truncated at that position with respect to the beam simulations.

The beam parameters for this subset of particles are summarized in Table II; all particles were accelerated to the exit without any further losses along the DTL.

Resulting normalized rms-emittance growth rates of 100% in longitudinal plane and of less than 16% in each transverse plane. By comparing with the matched case, it becomes clear that the deformed longitudinal input emittance in the laser generated distribution is a disadvantage: The longitudinal growth rate is even bigger than in the matched case, although the proton number in the beam is 43% only.

The transverse 90%, 99%, and 100% envelopes can be seen in Fig. 26. The optimized magnetic field gradients of the quadrupoles are ranging up to 50.8 T/m. The output particle distribution at the CH-structure exit in transverse

TABLE II. Normalized rms-emittance values for the input and output distribution of the laser generated case (216 mA).

Emittance	Input	Output
Transverse/mm mrad	x : 2.89	3.06
	y : 2.89	3.33
Longitudinal/keV ns	3.42	6.86

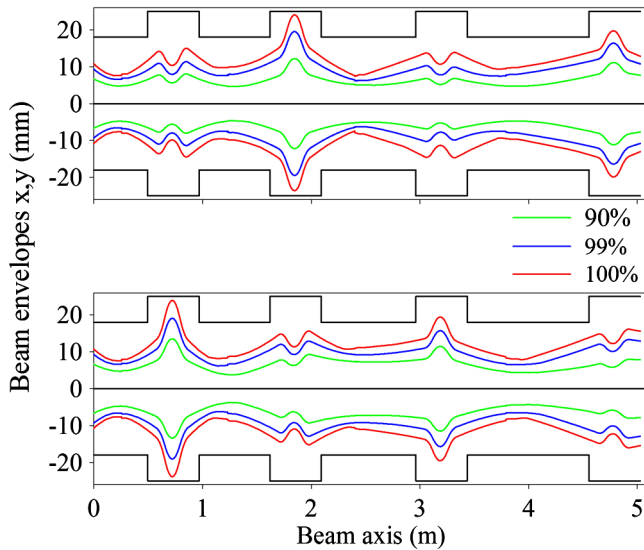


FIG. 26. Transverse 90%, 95%, and 100% beam envelopes starting 60 mm behind the solenoid. Black lines indicate the aperture.

and longitudinal planes are shown in Fig. 27 for 200 000 macroparticles.

These distributions are valid for further rf acceleration at acceptable loss rates, as the duty cycle for this kind of injector will stay very low.

B. rf power budget for a single bunch operation

One great advantage of high current, single bunch passage along the cavity is that the amplifier only has to provide the loss power in the cavity walls. The beam power is provided by the stored energy in the cavity fields, while reducing the field levels only within tolerances.

An estimation of the maximum single bunch proton number can be given in the following way: The stored field energy and thermic wall losses for any DTL cavity are given by the equations

$$W = \frac{P_{\text{loss}} \cdot Q_0}{\omega}; \quad (4)$$

$$P_{\text{loss}} = \frac{(N_G \cdot T_f \cdot V_0)^2}{Z_{\text{eff}} \cdot L}. \quad (5)$$

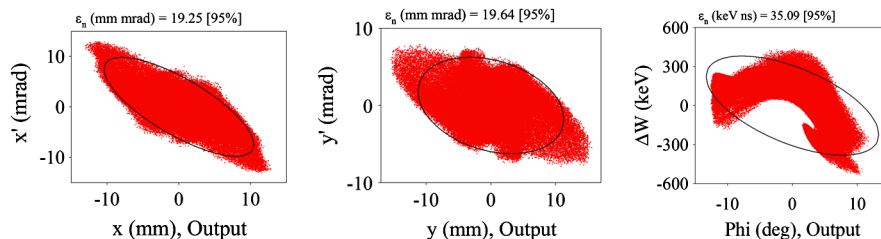


FIG. 27. Output transversal (left and middle) and longitudinal (right) particle distribution at the CH-DTL structure exit where the output energy is 40 MeV. The input particle distributions are shown in Fig. 25 (the red subset).

W = stored field energy, P_{loss} = thermic wall losses, Q_0 = unloaded quality factor, N_G = gap numbers, T_f = transit time factor, V_0 = gap voltage amplitude, Z_{eff} = effective shunt impedance, and L = effective cavity length.

The synchronous beam bunch will absorb cavity energy while passing N_G cells of length $\beta\lambda/2$; the bunch transit time along the cavity corresponds to

$$\tau_c = T \cdot \frac{N_G}{2} \quad (6)$$

with $T = 1/f$, f being the rf frequency in Hz. Assuming an rf phase of 0° in each gap center—that means maximum voltage gain $V_g = V_0 \cdot T_f$, the energy transfer to the beam bunch with N_p protons along each gap passage corresponds to

$$W_g = N_p \cdot e \cdot V_g. \quad (7)$$

The single bunch will pass the cavity during a few ten ns, where a feedback amplitude control will be too slow for compensation. On the other hand, a feed forward loop technique might provide solutions for achieving even higher bunch particle numbers, but is not considered here.

The acceptable voltage drop tolerance A caused by the bunch will be in the 1% to 2% range:

$$A = \left| \frac{\Delta V_{g,\text{max}}}{V_g} \right|. \quad (8)$$

This assures in a good approximation an unchanged power input P_l by the feeder line during the bunch passage; additionally the matching condition will be disturbed slightly only.

The time constant τ_m , after which the amplitude shift caused by the beam reaches the limit, is given by

$$\tau_m = 2 \cdot \frac{A \cdot W}{P_{b,\text{eff}}}. \quad (9)$$

$P_{b,\text{eff}}$ = the rf power extracted by the beam. In case of a single bunch passage through a $\beta\lambda/2$ structure it is

$$P_{b,\text{eff}} = 2 \cdot T_f \cdot V_0 \cdot \frac{Q_{\text{bunch}}}{T}. \quad (10)$$

The bunch particle limit will be exceeded if

$$\tau_m \leq \tau_c. \quad (11)$$

The particle limit is given by

$$\frac{\tau_m}{\tau_c} = 1; \quad (12)$$

$$\frac{2 \cdot A \cdot W}{T_f \cdot V_0 \cdot Q_{\text{bunch}} \cdot N_G} = 1; \quad (13)$$

$$Q_{\text{bunch}} = \frac{2 \cdot A \cdot W}{T_f \cdot V_0 \cdot N_G}. \quad (14)$$

As an example, for the first cavity of the proposed linac, cavity parameters can be estimated to get Q_{bunch} as follows:

$$L = 0.5 \text{ m}; \quad Z_{\text{eff}} = 60 \text{ M}\Omega/\text{m}; \quad N_G = 7 \text{ gaps}; \\ T_f = 0.8, \quad V_0 = 1.0 \text{ MV}; \quad Q_0 = 12\,500.$$

From Eq. (5), the wall losses result in $P_{\text{loss}} = 1.05 \text{ MW}$. Equation (4) gives the stored field energy $W = 6.4 \text{ J}$.

With an assumed tolerance value $A = 0.01$, one gets from Eq. (14) a maximum bunch charge of $Q_{\text{bunch}} = 2.29 \times 10^{-8} \text{ C}$, corresponding to a proton number $N_p = 1.43 \times 10^{11}$.

This would correspond to an equivalent beam current of 7.43 A.

This can be compared with a particle number of 4.3×10^9 in the simulate example VA 2.

This shows that the single bunch beam load will not affect the cavity oscillation, as stated above.

One further aspect is the total number of protons arriving at the linac entrance. These particles might cause cavity sparking when hitting the wall. Even cavity dephasing might occur by a large particle fraction with energies close enough to the accepted energy window. To reduce the risk of sparking, the intense low energy part of the laser generated pulse should be cut at the linac entrance by scrapers. Moreover, the inner drift tube contour can be optimized to reduce the secondary particle emission.

The total number of accepted particles with energies above 10.5 MeV is estimated to about 5×10^9 . But they are continuously distributed in rf phase. One main aspect of an rf postacceleration experiment will be the rf operation stability under these beam load conditions.

VI. CONCLUSIONS AND OUTLOOK

Laser driven proton beam sources have attractive features as rf linac injectors at energies above 10 MeV. They might become superior to the ion source, RFQ, and the first DTL stage of conventional linacs for special applications.

The high number of particles per bunch and the feature of delivering single bunches to the experiment are unique. Moreover, the beam power is delivered by the stored energy in the linac cavities and does not cause demand for larger rf amplifiers as in conventional linac systems.

Single bunch proton numbers around 10^{10} at the linac exit seem within reach. Detailed simulations from the

target through the solenoid and up to the linac entrance were presented, applying suitable software. Special care was taken on the time steps, in particular close to the target, and on the space charge interaction between electron and proton distributions.

The resulting emittance values in all 3 phase planes are relatively large at linac injection, due to the high phase space density at bunch generation which leads to emittance growth along the transport section.

A CH linac with high space charge limit and large transverse and longitudinal acceptance was designed to accept a maximum fraction of the laser generated proton bursts. The high particle number per bunch requires a very high voltage gain per meter along the linac to get enough longitudinal focusing force. The described example is at the upper technical limit. The voltage can be reduced by up to 50% with only a minor increase in emittance growth.

Attractive applications for single bunch operation as delivered naturally by laser driven systems might occur, involving time of flight techniques or the study of secondary reactions at low noise level, for instance.

The time averaged beam current at the linac exit may be increased to more interesting values for certain applications, if advanced laser systems with much higher repetition rates (100 Hz to several kHz) will become available. On the other hand, conventional injectors consisting of an ion source, low energy beam transport LEBT, and radio-frequency quadrupole RFQ will always be superior if a high time averaged proton current is needed, as these systems are flexible in the beam pulse structure up to cw operation.

With respect to the linac development it is intended to realize the first cavity of the proposed CH-DTL and to demonstrate the acceleration of a laser generated proton bunch.

ACKNOWLEDGMENTS

The authors appreciate the close and fruitful collaboration with the members of the PHELIX laser facility and our collaborators in the LIGHT project (GSI, Technische Universität Darmstadt, Helmholtz Institute Jena, and Forschungszentrum Dresden–Rossendorf). This work has been supported by HIC for FAIR within the LOEWE funding program of the state of Hesse.

-
- [1] E.L. Clark *et al.*, *Phys. Rev. Lett.* **84**, 670 (2000).
 - [2] R.A. Snavely *et al.*, *Phys. Rev. Lett.* **85**, 2945 (2000).
 - [3] S.C. Wilks, A.B. Langdon, T.E. Cowan, M. Roth, M. Singh, S. Hatchett, M.H. Key, D. Pennington, A. MacKinnon, and R.A. Snavely, *Phys. Plasmas* **8**, 542 (2001).
 - [4] J. Fuchs *et al.*, *Phys. Rev. Lett.* **94**, 045004 (2005).
 - [5] M. Roth *et al.*, *Laser Part. Beams* **23**, 95 (2005).

- [6] H. Schwoerer, S. Pfoth, O. Jäkel, K.-U. Amthor, B. Liesfeld, W. Ziegler, R. Sauerbrey, K. W. D. Ledingham, and T. Esirkepov, *Nature (London)* **439**, 445 (2006).
- [7] M. Roth *et al.*, *Plasma Phys. Controlled Fusion* **51**, 124039 (2009).
- [8] I. Hofmann *et al.*, in Proceedings of the 11th International Conference on Heavy Ion Accelerator Technology, Venice, Italy, 2009, FR-06, p. 213.
- [9] K. Harres *et al.*, *Phys. Plasmas* **17**, 023107 (2010).
- [10] D. Strickland and G. Mourou, *Opt. Commun.* **56**, 219 (1985).
- [11] M. D. Perry and G. Mourou, *Science* **264**, 917 (1994).
- [12] A. Schempp, *Nucl. Instrum. Methods Phys. Res., Sect. B* **45**, 302 (1990).
- [13] A. Schempp, in Proceedings of the 24th Linear Accelerator Conference, Victoria, BC, Canada, 2008, MO302, p. 41.
- [14] U. Ratzinger and R. Tiede, *Nucl. Instrum. Methods Phys. Res., Sect. A* **415**, 229 (1998).
- [15] U. Ratzinger *et al.*, in Proceedings of the 23rd Linear Accelerator Conference, Knoxville, Tennessee, USA, 2006, TH1004, p. 526.
- [16] V. Bagnoud *et al.*, *Appl. Phys. B* **100**, 137 (2009).
- [17] F. Nürnberg, A. Friedman, D. P. Grote, K. Harres, B. G. Logan, M. Schollmeier, and M. Roth, *J. Phys. Conf. Ser.* **244**, 022052 (2010).
- [18] U. Ratzinger, Habilitation treatise, Physics Department, Frankfurt University, Germany, 1998.
- [19] R. Tiede *et al.*, in Proceedings of the 10th European Particle Accelerator Conference, Edinburgh, Scotland, 2006 (EPS-AG, Edinburgh, Scotland, 2006), WEPCH 118, p. 2194.
- [20] J. M. Dawson, *Rev. Mod. Phys.* **55**, 403 (1983).
- [21] M. M. T. Wang and T. W. H. Sheu, *J. Comput. Appl. Math.* **79**, 147 (1997).
- [22] T. J. Stuchi, *Braz. J. Phys.* **32**, 958 (2002).
- [23] A. Almomani *et al.*, in Proceedings of the IPAC'10 Conference, Kyoto, Japan (ICR, Kyoto, 2010), THPD 035, p. 4355.
- [24] M. Reiser, *Theory and Design of Charged Particle Beams* (John Wiley & Sons, Inc., New York, 1994), pp. 106–110.
- [25] F. Nürnberg, Ph.D. thesis, Technische Universität Darmstadt, 2010.
- [26] H. Podlech, U. Ratzinger, H. Klein, C. Commenda, H. Liebermann, and A. Sauer, *Phys. Rev. ST Accel. Beams* **10**, 080101 (2007).
- [27] G. Clemente, U. Ratzinger, H. Podlech, L. Groening, R. Brodhage, and W. Barth, *Phys. Rev. ST Accel. Beams* **14**, 110101 (2011).
- [28] L. Groening *et al.*, in Proceedings of the 23rd Linear Accelerator Conference, Knoxville, Tennessee, USA, 2006, MOP061, p. 186.
- [29] G. Clemente *et al.*, in Proceedings of the 11th European Particle Accelerator Conference, Genoa, 2008 (EPS-AG, Genoa, Italy, 2008), WEPP079, p. 2701.
- [30] M. Steck, in Proceedings of the Workshop on Beam Cooling and Related Topics COOL'09, Lanzhou, China, 2009, THM1MCIO01, p. 98.
- [31] U. Ratzinger, *Nucl. Instrum. Methods Phys. Res., Sect. A* **464**, 636 (2001).
- [32] J. Broere *et al.*, in Proceedings of the 19th International Linear Accelerators Conference, Chicago, Illinois, 1998 (NTIS, Springfield, VA, 1998), p. 771.
- [33] P. Antici, M. Fazi, A. Lombardi, M. Migliorati, L. Palumbo, P. Audebert, and J. Fuchs, *IEEE Trans. Plasma Sci.* **36**, 1843 (2008).